CrystEngComm

ROYAL SOCIETY OF CHEMISTRY

PAPER

View Article Online
View Journal | View Issue

Cite this: *CrystEngComm*, 2022, **24**, 5588

Controllability of β-Ga_2O_3 single crystal conductivity by V doping†

Pengkun Li,[ab] Xueli Han,[ab] Duanyang Chen,*[a] Qinglin Sai[a] and Hongji Qi*[ac]

Received 25th March 2022,
Accepted 11th July 2022

DOI: 10.1039/d2ce00418f

rsc.li/crystengcomm

The introduction of different elements into semiconductors to achieve conductivity control of n-type doping has considerable scientific significance and practical application prospects, which can further promote their extensive application in the field of electronic devices. Herein, a series of V-doped beta-gallium oxide (β-Ga_2O_3) single crystals with different concentrations were cultivated using the optical floating zone method. The influence of V doping on the structural, electrical, and optical properties of β-Ga_2O_3 single crystals was systematically investigated. The characterization results revealed that V-doped β-Ga_2O_3 single crystals exhibited superior crystalline quality; moreover, the free carrier concentration increased from 6.9×10^{16} cm^{-3} to 6.4×10^{18} cm^{-3} and then decreased to 3.1×10^{16} cm^{-3} with an increase in the V concentration. The optical transmission of the crystals initially decreased in the infrared region and then increased, which is related to the change in the conductive electrons. The intensities of the two absorption peaks located at approximately 400 nm and 610 nm increased with increasing V doping concentration. From the Raman scattering spectra, the inhibition of V on the [$Ga_{II}O_6$] octahedral peak intensity became evident with increasing V content. These valuable findings may contribute to the research on β-Ga_2O_3-based electronic and optical devices.

Published on 14 July 2022. Downloaded on 9/10/2022 9:58:10 AM.

1. Introduction

The continuous development of materials, has enabled the application of semiconductors in photodetectors,[1,2] solar cells,[3,4] light-emitting diodes,[5,6] and various other fields.[7–9] Beta-gallium oxide (β-Ga_2O_3) crystals, as an outstanding representative of the emerging semiconductors, have been increasingly applied in semiconductor fields such as high-power electronic devices,[10] ultraviolet detectors,[11] and gas sensors[12] largely owing to their excellent material properties.

β-Ga_2O_3, with an ultra-wide bandgap of 4.8–4.9 eV at room temperature, belongs to a class of materials called transparent semiconducting oxides. It has a high theoretical critical electric field of 8 MV cm^{-1} and a Baliga's figure-of-merit of 3444, which is more than 10 times that of SiC.[13] Compared to other broad-bandgap materials such as SiC, GaN, and diamond, β-Ga_2O_3 has a large size and enables the production of high-quality single-crystal substrates, which can be fabricated utilizing melt growth methods including Czochralski (CZ),[14,15] vertical Bridgman (VB),[16] edge-defined film-fed growth (EFG),[17,18] and floating-zone (FZ) methods,[19,20] The β-Ga_2O_3 crystal with the largest volume has been grown using the CZ method by far.[15,21,22] 2 inch diameter (100) β-Ga_2O_3 and 1 inch β-Ga_2O_3 crystals with different orientations were grown by VB.[23,24] The largest β-Ga_2O_3 bulk crystal (6 inch) was obtained using the EFG method.[25] In the FZ method, crystals growing in different directions and 1 inch crystal have been demonstrated.[19] Among these growth methods, the FZ process with cost effective, convenient operation and short growth period can be used to prepare high-quality intrinsic or doped β-Ga_2O_3 single crystals.

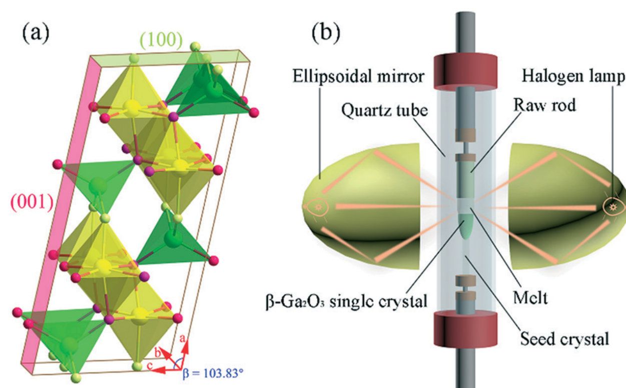

Fig. 1 (a) β-Ga_2O_3 crystal structure. (b) Schematic of the OFZ experimental device for the growth of β-Ga_2O_3 single crystals.

[a] Key Laboratory of Materials for High Power Laser, Shanghai Institute of Optics and Fine Mechanics, Chinese Academy of Sciences, Shanghai 201800, China. E-mail: chenduanyang@siom.ac.cn, qhj@siom.ac.cn
[b] Center of Materials Science and Optoelectronics Engineering, University of Chinese Academy of Sciences, Beijing 100049, China
[c] Hangzhou Institute of Optics and Fine Mechanics, Hangzhou 311421, China

† Electronic supplementary information (ESI) available. See DOI: https://doi.org/10.1039/d2ce00418f

This journal is © The Royal Society of Chemistry 2022

Published on 14 July 2022. Downloaded on 9/10/2022 9:58:10 AM.

A schematic of the unit cell of β-Ga_2O_3 is illustrated in Fig. 1(a). β-Ga_2O_3 has a monoclinic structure (space group *C*2/*m*), and the cell parameters are a = 12.214 Å, b = 3.0371 Å, c = 5.7981 Å, and β = 103.83°.[26] The gallium ions are located at [Ga_IO_4] tetrahedral and [$Ga_{II}O_6$] octahedral sites. Therefore, the gallium atoms in the crystal have tetra- and hexa-coordination. The double chains composed of the [$Ga_{II}O_6$] octahedrons in the crystal are arranged along the *b*-axis, and the two adjacent chains are connected by the [Ga_IO_4] tetrahedrons.[26] In addition, there are two easy cleavage planes in β-Ga_2O_3 crystal, which are the (100) and (001) planes.

As with other semiconductors, dopants are typically used in β-Ga_2O_3 crystals to alter their material properties. Electrical conductivity is one of the most important properties of β-Ga_2O_3 in device applications. Several studies have reported an increase in the carrier concentration of β-Ga_2O_3 through the introduction of high-valence elements (Si, Sn, Nb, Ta, W, *etc.*) for effective n-type doping.[27–31] V is typically doped into TiO_2 for photocatalytic research.[32,33] Considering the ionic radius, the radius of V^{5+} (0.059 nm) is nearly the same as that of Ga^{3+} (0.062 nm), and V slightly changes the lattice size of β-Ga_2O_3 single crystals. V with five valence electrons can produce more free carriers. Therefore, V is a suitable dopant. In addition, the regulation of V on the electrical properties of β-Ga_2O_3 single crystals has not been reported. Consequently, it is of great significance to comprehend the electrical and optical properties of V-doped β-Ga_2O_3 crystals.

In this paper, a convenient optical floating zone (OFZ) approach was introduced for the growth of β-Ga_2O_3 single crystals doped with different V concentrations. The microstructure, surface morphology, conductivity, chemical states, optical bandgap, and V^{5+} ion substitution position of V-doped β-Ga_2O_3 were investigated through high-resolution X-ray diffraction, atomic force microscopy, laser confocal microscope system, Hall, X-ray photoelectron spectroscopy, optical transmission, and Raman scattering techniques. Interesting discoveries such as the initial increase and subsequent reduction in carrier concentration with an increase in the V doping concentration, as well as the two absorption peaks in the transmission spectra, are expected to further broaden the application prospects of β-Ga_2O_3 in electronic and optical devices.

2. Materials and methods

2.1 Preparation of single crystals

An OFZ growth chamber with two halogen lamps and ellipsoidal mirrors was employed to grow a series of single-crystalline V-doped β-Ga_2O_3 samples with different V concentrations (undoped, 0.05 mol%, 0.10 mol%, 0.20 mol%, 0.50 mol%, 1.00 mol%), as shown in Fig. 1(b). The two halogen lamps were located at the respective focal points of the ellipsoids on both sides. Prior to the OFZ growth, raw rods were prepared from Ga_2O_3 powder (99.9999%) and V_2O_5 powder (99.99%), and pressed into cylinders using a cold isostatic press. Subsequently, the rods were annealed under air at 1450 °C for 20 h, and the [010]-oriented β-Ga_2O_3 single crystals were used as the seeds. Then, the raw rod and seed crystals were fixed on the upper and lower rotating rods, respectively. Under the reflection of the ellipsoid mirrors, the light was focused on the contact position between the lower end of the raw rod and the upper portion of the seed crystal. After reaching a certain temperature, the raw rod and seed crystal started to melt, and the melted part formed a stable melting zone through docking. Finally, with the slow descent of the upper and lower rotating rods, V-doped β-Ga_2O_3 single crystals were gradually formed on the seeds at a rate of 5 mm h^{-1} and cooled naturally to room temperature under dry air flow. The crystals were grown in the direction ([010]) of the seed crystal. Wafers parallel to the (100) plane were processed for subsequent testing.

2.2 Characterization methods

In order to minimize or even eliminate the influence of the inhomogeneity of the V element in the crystal growth direction, the top crystal (at the same position) of each sample was selected for processing and testing. The crystal structure and quality of the as-synthesized samples were determined by X-ray diffraction (XRD, Bruker D8 ADVANCE, Cu Kα line, operated at 40 kV and 40 mA). The X-ray powder diffraction patterns and X-ray diffraction rocking curves were obtained, respectively. The morphologies of the single-crystal substrates were investigated by atomic force microscopy (AFM, CSPM 5500) and a laser confocal microscope system (LCM, ZEISS LSM900). The electrical properties measurements were carried out utilized the Van der Pauw method (Lake Shore 8404 Hall system) at room temperature. The optical transmittance (OT) spectra were measured using a PerkinElmer Lambda 1050+ UV/VIS/NIR spectrometer. The chemical states of the samples were characterized by X-ray photoelectron spectroscopy (XPS, ESCALAB 250Xi). The room-temperature Raman spectra were collected using a Horiba iHR550 spectrometer with a laser beam under excitation sources of 633 nm.

3. Results and discussion

3.1 Structure characterization

Fig. 2(a) shows the as-grown Ga_2O_3 crystals. The transparent Ga_2O_3 crystals without cracks had lengths of approximately 35–45 mm and diameters ranging from 4 mm to 5 mm. The color of the Ga_2O_3 considerably varied among the undoped and V-doped crystals. The undoped Ga_2O_3 crystal showed pale blue, whereas the V-doped Ga_2O_3 crystals appeared emerald green. As the concentration of V increased, the green color gradually became more prominent.

XRD was utilized to identify the structures of the as-synthesized Ga_2O_3 crystals. The powder XRD patterns of the

This journal is © The Royal Society of Chemistry 2022

Published on 14 July 2022. Downloaded on 9/10/2022 9:58:10 AM.

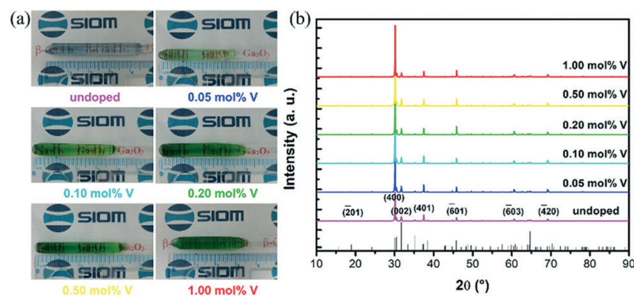

Fig. 2 (a) Undoped and V-doped β-Ga_2O_3 single crystals. (b) XRD patterns of undoped and V-doped β-Ga_2O_3 single crystals. The standard JCPDF card (No. 41-1103) is located at the bottom for comparison.

as-prepared crystals are shown in Fig. 2(b). The positions of all the sharp diffraction peaks were indexed to the standard β-Ga_2O_3 crystal JCPDF card (No. 41-1103), and no diffraction peaks of other impurities were observed in any of the products. It is clear that the dopant did not alter the crystal structure, and the V-doped β-Ga_2O_3 crystals maintained the monoclinic structure. These diffraction peaks with strong intensity shifted to larger 2-theta angle with the increase of V concentration (as shown in Fig. S2†), indicating that the doping of V with small ion radius decreased the lattice parameters.

The actual percentage of V content in the samples were assessed by ICP analysis, as shown in Table 1. Obviously, the actual content in the raw material was less than the nominal content due to impurity segregation throughout the growth process.

3.2 Crystal quality

The crystalline quality of the V-doped β-Ga_2O_3 crystal was evaluated using high-resolution X-ray diffraction. The illustration in Fig. 3(a) shows the polished 0.20 mol% V-doped β-Ga_2O_3 single-crystal substrate, which had a size of approximately 5 mm × 7 mm. The β-Ga_2O_3 single crystal substrates with undoped and other V-doped concentrations are shown in Fig. S1.† Fig. 3(a) shows the corresponding rocking curve of the 0.20 mol% V-doped β-Ga_2O_3 crystal (400) plane. Rocking curves of the other V-doped β-Ga_2O_3 single crystals are shown in Fig. S3.† With the increase of V concentration, the full-width at half-maximum (FWHM) of crystals increased and the diffraction peaks shifted to larger diffraction angle based on Bragg equation. This is consistent with the results of the powder XRD, which can be attributed to the partial replacement of Ga^{3+} (0.062 nm) by V^{5+} (0.059 nm) with a smaller ionic radius. The FWHM values of the sharp and symmetrical diffraction peaks were all less than 152 arcsec. Limited by the heating mode, the OFZ-grown β-Ga_2O_3 crystals have larger FWHM values than those of the EFG and Czochralski methods. However, among the β-Ga_2O_3 crystals grown by OFZ technique, the V-doped β-Ga_2O_3 single crystals in our work have a high crystallization quality without sub-grain boundaries.

The LCM and AFM images of 0.20 mol% V-doped β-Ga_2O_3 single crystals are shown in Fig. 3(b–d). Similarly, the LCM and AFM images of the β-Ga_2O_3 single-crystal samples with other V concentrations are shown in Fig. S4 and S5.† From the two-dimensional (2D, Fig. 3(b) and S4(a–e)†) and three-dimensional (3D, insets of Fig. 3(b) and S4(f–j)†) LCM images, it can be seen that the undoped and V-doped β-Ga_2O_3 single crystals have smooth surfaces. AFM measurements were performed in tapping mode on a sample surface area of 5 × 5 μm^2 (Fig. 3(c and d) and S5(a–j)†). The results indicate that the surface topography morphologies of the single-crystal substrates were clear and the root-mean-square (RMS) values of surface roughness were all less than 0.5 nm, implying that the prepared undoped and V-doped β-Ga_2O_3 have quite flat surfaces. Such ultra-smooth surface indicated that processing technology of the crystal was excellent, which provides a guarantee for the subsequent testing and preparation of high-performance devices.

Table 1 ICP data of the β-Ga_2O_3 single crystals with different doping concentrations

	Sam. 1	Sam. 2	Sam. 3	Sam. 4	Sam. 5
Doping (mol%)	0.05	0.10	0.20	0.50	1.00
ICP (mol%)	0.025	0.046	0.099	0.119	0.177

3.3 Basic electrical properties

Electrical properties are key factors for evaluating the suitability of oxide materials in the field of electronic devices, for instance Schottky barrier diodes and field-effect transistors. All the obtained β-Ga_2O_3 bulk single crystals exhibited n-type semiconductors or electro-insulating states.

Fig. 4(a–c) show the variation in the carrier concentration, mobility, and electrical resistivity of the V-doped β-Ga_2O_3 single crystal with different V doping concentrations, respectively, and the specific values are listed in Table 2. A 20 nm Ti/100 nm Al layer was evaporated on the four corner surfaces of the samples. This was followed by rapid annealing at 500 °C in the N_2 environment for ohmic contact. All the samples exhibited n-type conduction. The carrier concentration of the undoped β-Ga_2O_3 single crystal was 6.90

Table 2 Hall data at room temperature of the β-Ga_2O_3 single crystals with different V doping concentrations

V content (mol%)	Type	Carrier concentration (cm^{-3})	Mobility (cm^2 (V^{-1} s^{-1}))	Resistivity (Ω cm)
0.00	N	6.90×10^{16}	150.0	0.597
0.05	N	2.10×10^{18}	91.0	0.0322
0.10	N	2.80×10^{18}	81.0	0.02763
0.20	N	6.40×10^{18}	70.0	0.0139
0.50	N	3.97×10^{18}	67.9	0.02318
1.00	N	3.10×10^{16}	7.2	28

This journal is © The Royal Society of Chemistry 2022

Published on 14 July 2022. Downloaded on 9/10/2022 9:58:10 AM.

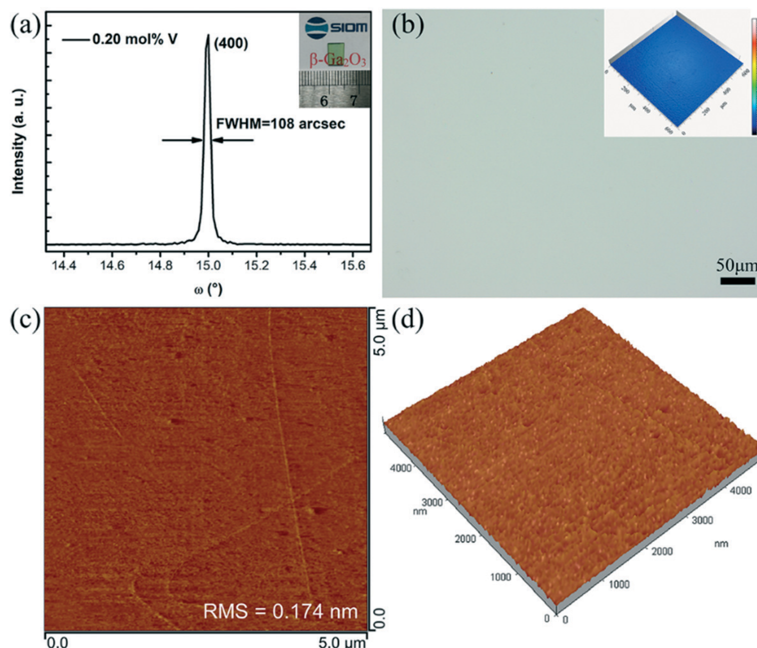

Fig. 3 (a) XRD rocking curve, (b) 2D LCM, (c) 2D AFM, and (d) 3D AFM surface morphologies of 0.20 mol% V-doped β-Ga_2O_3 single crystal. Inset of panel in (a) shows the polished V-doped β-Ga_2O_3 (100) single-crystal substrate (5 mm × 7 mm). Inset in panel (b) displays a 3D LCM image of the 0.20 mol% V-doped β-Ga_2O_3 crystal.

× 10^{16} cm^{-3}, owing to the existence of impurities such as Si and other shallow-level donors.

It is interesting to note that the carrier concentration in the β-Ga_2O_3 crystal increased from 6.9 × 10^{16} cm^{-3} to 6.4 × 10^{18} cm^{-3}, and then decreased to 3.1 × 10^{16} cm^{-3} with an increase in the V concentration (as shown in Fig. 4(a)). The electron mobility continuously decreased with increasing V doping concentration (Fig. 4(b)). The mobility in β-Ga_2O_3 changed by nearly two orders of magnitude, from 1.5 × 10^2 cm^2 V^{-1} s^{-1} to 7.2 × 10^0 cm^2 V^{-1} s^{-1}. It was found that the electrical resistivity initially decreased gradually from 0.597 Ω cm to 0.0139 Ω cm and then significantly increased to 28 Ω cm with an increase in the V doping concentration, which is exactly the opposite of the change tendency of the carrier concentration (Fig. 4(c)).

When incorporated with a small amount of V (0–0.20 mol%), the number of V atoms effectively replacing Ga in the lattice increased gradually, which significantly contributed to the carriers of the crystal. Consequently, the electron concentration increased with the incorporation of V, and the resistivity gradually reduced. The scattering of electron by doped V was enhanced, resulting in the decrease of carrier mobility. By further increasing the amount of V doping (>0.20 mol%), the solid solubility of V in β-Ga_2O_3 was near the limit, and the excess V atoms could not replace Ga in the lattice, and then segregated in local regions and formed non-conductive V_xO_y clusters, which no longer provided electrons, similar to Al or Nb doped ZnO,[34,35] in turn leading to an increase in the degree of crystal disorder, acting as an electron trap. This undoubtedly obstructed the effective free electron conduction. Accordingly, the carrier concentration decreased with a further increase in the V content, and the resistivity of β-Ga_2O_3 also seemed to increase. This phenomenon was reported in V-doped ZnO.[36] The dopant concentration in β-Ga_2O_3 crystal is not "more is better." The maximum doping is achieved at the supersaturated dopant concentration above the solubility limit, that is, when thermodynamically favored for the exsolution of the

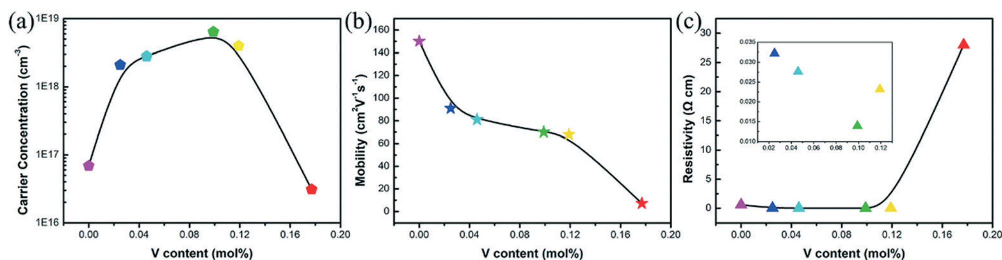

Fig. 4 (a) Carrier concentration, (b) mobility and (c) electrical resistivity of the undoped and V-doped β-Ga_2O_3 single crystals. The V content as measured by the ICP was used as the *X*-axis.

dopant.[37] However, excessive doping levels would unnecessarily advance the nucleation of secondary phase (*e.g.*, V_xO_y). The mobility further decreased with an increase in V content, which was mainly caused by the gradual enhancement of ionized impurity scattering within the crystal.

The activation ratios of Si and Sn atoms used as donors in β-Ga_2O_3 bulk crystals grown by OFZ method were 25–50% and 26%, respectively.[38,39] The activation ratio of V element in the nominal 0.05–0.20 mol% V-doped β-Ga_2O_3 (*i.e.*, the ratio of carrier concentration to V concentration measured by ICP) varied between approximately 16% and 22% by calculation. When the doping concentration of V exceeds 0.20 mol%, many electron traps existed in the crystal, resulting in a significant reduction in the activation ratio of V in the β-Ga_2O_3 crystal to about 0–9%. The activation ratio of V element is lower than that of Si and Sn elements. The reason for this discrepancy should be further investigated.

3.4 XPS analysis

The chemical composition of the samples and the chemical valence states of the elements in the materials were obtained through XPS characterization. To study whether the valence state of V changed in V-doped β-Ga_2O_3 single crystal, XPS tests and analyses were performed. Considering the detection limit of XPS equipment, we chose to use 1.00 mol% V-doped β-Ga_2O_3 single crystal for testing. The results were fitted by Gaussian–Lorentzian deconvolution, as shown in Fig. 5. The typical XPS survey spectrum of the 1.00 mol% V-doped β-Ga_2O_3 sample revealed the Ga XPS peaks, O XPS peak, Ga Auger peaks (Ga LMM), O Auger peak (O KLL), V XPS peak, and C peak in the energy range from 0 to 1300 eV, as shown in Fig. 5(a). Fig. 5(b)–(d) show the high-resolution XPS spectra of Ga 3d and O 2s, O 1s, Ga LMM, and V 2p, respectively. The binding energy was calibrated utilizing the 284.8 eV carbon peak (C 1s).

Fig. 5(b) shows the XPS scan of the Ga 3d and O 2s regions of the 1.00 mol% V-doped β-Ga_2O_3 single crystal. The photoemission of Ga 3d were located at 19.38 eV and 20.70 eV and overlapped with the binding energy peak of O 2s centered at 23.51 eV. The peak at 19.38 eV was attributed to Ga^+, and the 20.70 eV (Ga^{3+}) main peak was ascribed to the Ga–O bond in the Ga_2O_3 crystals.[40,41] The energy difference between the two peaks of Ga^{3+} and Ga^+ is 1.32 eV, which corresponds to the previous research results.[41,42] The detailed O 1s XPS spectrum with two fitted peaks is depicted in Fig. 5(c). The peak with a binding energy centered at 531.44 eV was identified as O bonded to Ga in Ga_2O_3.[40,43] Whereas the other peak located at 532.63 eV was determined as C–O, indicating that C has been adsorbed as an impurity on the sample surface or into the lattice during the growth process.[44,45]

Fig. 5(d) shows the high-resolution XPS spectra of Ga LMM and V 2p. XPS scan of Ga LMM-V 2p operated in CAE mode with a passing energy of 30 eV and a step size of 0.10 eV. The peak of Ga LMM overlapped with that of V 2p. The two peaks located at 519.42 and 518.52 eV correspond to Ga LMM and V^{5+} $2p_{3/2}$, respectively.[46,47] Moreover, the valence state of the V element in the 1.00 mol% V-doped β-Ga_2O_3 single crystal remained unchanged and still maintained a +5 valence. It is reported that V-doped β-Ga_2O_3 films contain V^{5+} and V^{4+} ions, and V^{5+} ions accounted for a high proportion. The XPS peak of V^{4+} ion is not shown in Fig. 5(d), which may be due to the low content of V^{4+} exceeding the lower detection limit of XPS equipment. Both V^{4+} and V^{5+} ions

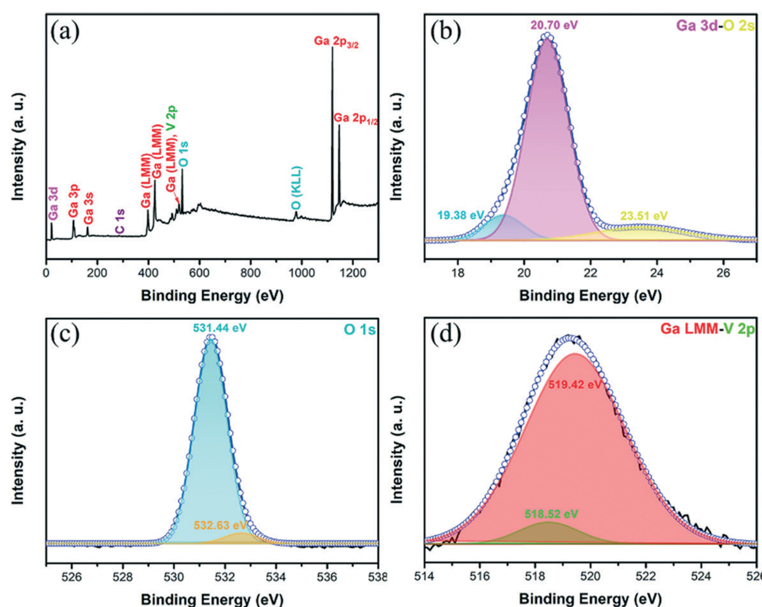

Fig. 5 (a) XPS survey spectrum of 1.00 mol% V-doped β-Ga_2O_3 single crystal. High-resolution XPS spectra of (b) Ga 3d and O 2s, (c) O 1s and (d) Ga LMM and V 2p.

Published on 14 July 2022. Downloaded on 9/10/2022 9:58:10 AM.

This journal is © The Royal Society of Chemistry 2022

Published on 14 July 2022. Downloaded on 9/10/2022 9:58:10 AM.

provided free electrons for β-Ga_2O_3 single crystals. Hence, the results further indicate that more carriers were trapped owing to the increase in the degree of crystal disorder, which led to an abnormal carrier concentration of the β-Ga_2O_3 single crystal doped with a high V concentration.

3.5 Basic optical properties

The optical properties of the V-doped β-Ga_2O_3 single crystals strongly depended on the carrier concentration in the crystals. Consequently, the V content largely determined the optical properties of the β-Ga_2O_3 single crystals. Fig. 6(a) and S6† exhibit the optical transmission spectra of undoped and V-doped β-Ga_2O_3 single crystals grown by OFZ. The highest transmittance was observed at approximately 80% in the visible wavelength region. Compared with undoped β-Ga_2O_3 crystal, V-doped β-Ga_2O_3 crystals introduced two wide absorption bands located near 400 and 610 nm, respectively (Fig. 6(a) and S5†), whose transmission intensity decreased with an increase in the concentration of V in the crystals, similar to that as in the Cr-doped β-Ga_2O_3.[22,48] V-doped β-Ga_2O_3 appeared green, indicating that part of V entered the crystal in the valence state of +3.[49] These two absorption peaks may be caused by the crystal field splitting electron transitions of V^{3+} and V^{4+} in β-Ga_2O_3.[50] Since V^{5+} has no 3d electrons (3d0 configuration), it does not contribute to the central absorption of two broadband forms in the visible region.

The change curve of transmittance in the infrared (IR) region (λ = 2000 nm) with the increase in the V component is shown in Fig. 6(b). In the range of 0–0.20 mol%, the transmittance in the IR region gradually attenuated, indicating that the effective carrier concentration in the β-Ga_2O_3 single crystals increased with V doping. What is more noteworthy is that the transmittance in the IR region increased when the amount of V exceeded 0.20 mol%. The transmittance of the 1.00 mol% V-doped β-Ga_2O_3 crystal in the IR region was comparable to that of the undoped β-Ga_2O_3, indicating that the effective free carrier concentration in the β-Ga_2O_3 crystals decreased (V content > 0.2 mol%). This is in accordance with the results of the carrier concentration data (Fig. 4(a)).

Fig. 6(c) shows the curves of $(\alpha h\nu)^2$ changing with the photon energy ($h\nu$) according to the tested absorption coefficient (α), which is expressed as a function of the incident light wavelength (λ). Considering the functional relationship between α and the band gap, we extracted the estimated values of the band gap of V-doped β-Ga_2O_3 varying with V content, as shown in Fig. 6(d). The optical band-gap gradually decreased with the increasing V composition, which may be due to an increase in the density of the localized state in the conduction band.[30] As expressed by the following equation:

$$E_g = -\frac{3q^2}{16\pi\varepsilon}\sqrt{\frac{q^2N}{\varepsilon kT}} \tag{1}$$

where N is the density of the localized state, ε is the dielectric constant, q is the electronic charge (C), k is the Boltzmann's constant (J K^{-1}), and T is the temperature (K).

Fig. 7 shows the room-temperature Raman spectra of the undoped and V-doped β-Ga_2O_3 single crystals between 100 and 1000 cm^{-1}. Nine phonon mode peaks were detected, derived from the undoped and V-doped β-Ga_2O_3 crystals, which coincided with the data in the literature.[30,41] These

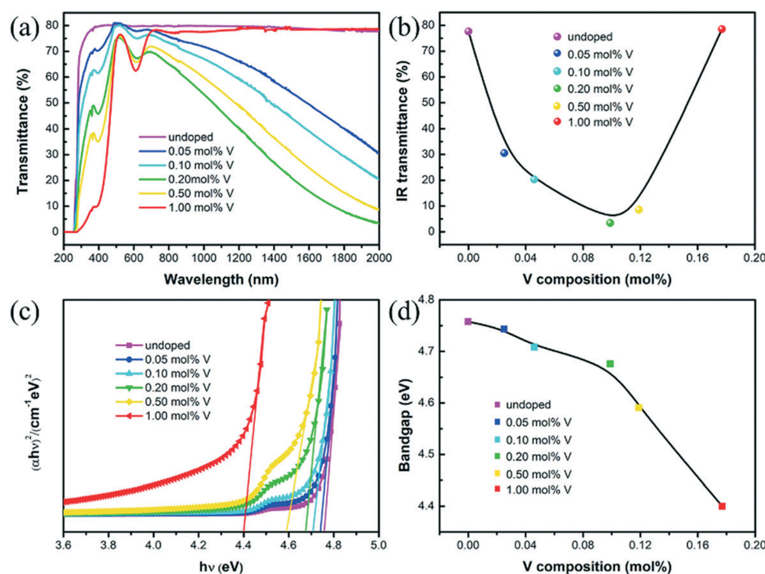

Fig. 6 (a) Room-temperature optical transmission spectra for the undoped and V-doped β-Ga_2O_3 single crystals. (b) The points reveal the variation of the transmittance in the IR region (λ = 2000 nm) with V composition. (c) $(\alpha h\nu)^2$ curves as a function of photon energy ($h\nu$); α represents the absorption coefficient. (d) The dots describe that the band gap extracted by (c) varies with the V composition. For (b) and (d), the V composition measured by the ICP was used as the X-axis.

Published on 14 July 2022. Downloaded on 9/10/2022 9:58:10 AM.

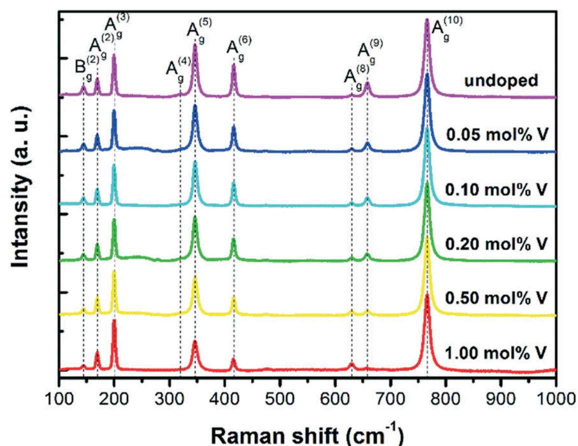

Fig. 7 Raman spectra of undoped and V-doped β-Ga_2O_3 single crystals.

peaks were located in $B_g^{(2)}$: 144 cm^{-1}, $A_g^{(2)}$: 169 cm^{-1}, $A_g^{(3)}$: 199 cm^{-1}, $A_g^{(4)}$: 320 cm^{-1}, $A_g^{(5)}$: 345 cm^{-1}, $A_g^{(6)}$: 416 cm^{-1}, $A_g^{(8)}$: 629 cm^{-1}, $A_g^{(9)}$: 658 cm^{-1}, and $A_g^{(10)}$: 766 cm^{-1}, and could be divided into three groups:[51,52] the primary-frequency phonon modes ($B_g^{(2)}$, $A_g^{(2)}$ and $A_g^{(3)}$) are related to vibrations and translations of the [Ga_IO_4] tetrahedral chains; the secondary-frequency phonon modes ($A_g^{(4)}$, $A_g^{(5)}$ and $A_g^{(6)}$) are attributed to the deformation of the [Ga_IO_4] tetrahedron and [$Ga_{II}O_6$] octahedron; and the third-frequency phonon modes ($A_g^{(8)}$, $A_g^{(9)}$ and $A_g^{(10)}$) are assigned to the stretching and bending of the [Ga_IO_4] tetrahedron. The addition of V atoms significantly inhibited $A_g^{(4)}$, $A_g^{(5)}$ and $A_g^{(6)}$ (as shown in Fig. 7), indicating that V ions mainly substituted Ga^{3+} at the center of the octahedron.

More accurate shifting information of the Raman peaks measured in the experiment was obtained through the Lorentz fit equation, as listed in Table 3. Most phonon mode peaks exhibited a slight positive shift after the addition of V. This is ascribed to the partial replacement of the Ga^{3+} ion (0.062 nm) with a larger ion radius by the smaller V^{5+} ion (0.059 nm), resulting in lattice contraction and reduction of the bond length (l). The relationship between the bond length and phonon frequency (ω) is inversely proportional

Table 3 Raman scattering spectra of undoped and V-doped β-Ga_2O_3 single crystals

	Peak position (cm^{-1})					
	Undoped β-Ga_2O_3	V-doped β-Ga_2O_3 (mol%) 0.05	0.10	0.20	0.50	1.00
$B_g^{(2)}$	143.732	144.244	143.768	144.180	144.127	144.389
$A_g^{(2)}$	169.122	169.140	169.128	169.208	169.167	169.163
$A_g^{(3)}$	199.660	199.743	199.705	199.860	199.742	199.863
$A_g^{(4)}$	318.834	—	—	—	—	—
$A_g^{(5)}$	346.192	346.232	346.313	346.375	346.297	346.375
$A_g^{(6)}$	416.129	416.141	416.141	415.963	416.150	415.826
$A_g^{(8)}$	629.607	629.616	629.571	629.900	629.594	629.772
$A_g^{(9)}$	658.072	658.398	658.291	657.968	658.427	658.536
$A_g^{(10)}$	766.160	766.276	766.290	766.277	766.350	766.335

and can be expressed as $\omega \sim l^{-\sqrt{1/2}}$.[41] Consequently, a decrease in the bond length corresponds to an increase in the phonon frequency.

4. Conclusions

In conclusion, we proposed a strategy for using V as a dopant to realize the tunability of the electrical resistivity and carrier concentration of β-Ga_2O_3. Doped β-Ga_2O_3 crystals with different V contents were successfully prepared using the optical float zone method. The powder and high-resolution XRD results demonstrated that the as-synthesized V-doped β-Ga_2O_3 samples with different concentrations consisted of monoclinic (*C*2/*m*) single crystals with high crystalline quality. As the V concentration increased, the carrier concentration of V-doped β-Ga_2O_3 crystals increased from 6.9 × 10^{16} cm^{-3} to 6.4 × 10^{18} cm^{-3}, and then reduced to 3.1 × 10^{16} cm^{-3}; and the resistivity gradually decreased from 0.597 Ω cm to 0.0139 Ω cm, and then increased sharply to 28 Ω cm. This is attributed to the formation of electron traps in the crystal when the V content exceeds a certain value, resulting in an abnormality in the carrier concentration and resistivity. In the transmission spectra, with the incorporation of V, two absorption peaks appeared at about 400 and 610 nm, and the intensity of the absorption peaks enhanced with increasing V content. Raman scattering revealed that the V ion mainly substituted the Ga^{3+} ion at the center of the octahedron. This is expected to promote extensive applications of β-Ga_2O_3 in electronic and optoelectronic devices.

Conflicts of interest

There are no conflicts interest to declare.

Acknowledgements

We would like to thank Hangzhou Fujia Gallium Technology Co., Ltd. for its help in crystal growth, processing and testing. The authors gratefully acknowledge the financial support of this work by the National Natural Science Foundation of China (grant number 51972319), the Shanghai Science and Technology Commission (grant number 20511107400), and the Youth Innovation Promotion Association, Chinese Academy of Science (CAS) (grant number 2021245).

References

1 J. Wang, C. Chu, K. Tian, J. Che, H. Shao, Y. Zhang, K. Jiang, Z.-H. Zhang, X. Sun and D. Li, *Photonics Res.*, 2021, **9**, 734–740.
2 H. Lee, J. H. Mun, I. Oh, K. Beom, T.-S. Yoon, A. R. Hong, H. S. Jang and D. H. Kim, *Mater. Charact.*, 2021, **171**, 110813.
3 M. Samykano, *Mater. Charact.*, 2021, **179**, 111373.
4 I. M. A. Mohamed, V.-D. Dao, A. S. Yasin, H. M. Mousa, M. A. Yassin, M. Y. Khan, H.-S. Choi and N. A. M. Barakat, *Mater. Charact.*, 2017, **127**, 357–364.

This journal is © The Royal Society of Chemistry 2022

Published on 14 July 2022. Downloaded on 9/10/2022 9:58:10 AM.

5 L. Guo, K. Jiang, X. Sun, Z. Zhang, J. Ben, Y. Jia, Y. Wang and D. Li, *Photonics Res.*, 2021, **9**, 1907–1915.
6 M. Tian, C. Ma, T. Lin, J. Liu, D. N. Talwar, H. Yang, J. Cao, X. Huang, W. Niu, I. T. Ferguson, L. Wan and Z. C. Feng, *J. Mater. Sci.*, 2020, **56**, 1481–1491.
7 S. Zhang, Y. Li, P. Hu, Z. Tian, Q. Li, A. Li, Y. Zhang and F. Yun, *Photonics Res.*, 2021, **9**, 432–438.
8 W. Tian, F. Liang, D. Lu, H. Yu and H. Zhang, *Photonics Res.*, 2021, **9**, 317–323.
9 J. Reiprich, N. A. Isaac, L. Schlag, M. Hopfeld, G. Ecke, T. Stauden, J. Pezoldt and H. O. Jacobs, *Cryst. Growth Des.*, 2019, **19**, 6945–6953.
10 T. Harada, S. Ito and A. Tsukazaki, *Sci. Adv.*, 2019, **5**, eaax5733.
11 Z. Y. Wu, Z. X. Jiang, C. C. Ma, W. Ruan, Y. Chen, H. Zhang, G. Q. Zhang, Z. L. Fang, J. Y. Kang and T. Y. Zhang, *Mater. Today Phys.*, 2021, **17**, 100356.
12 Q. N. Abdullah, A. R. Ahmed, A. M. Ali, F. K. Yam, Z. Hassan and M. Bououdina, *Int. J. Hydrogen Energy*, 2021, **46**, 7000–7010.
13 M. Higashiwaki, K. Sasaki, A. Kuramata, T. Masui and S. Yamakoshi, *Appl. Phys. Lett.*, 2012, **100**, 013504.
14 Y. Tomm, P. Reiche, D. Klimm and T. Fukuda, *J. Cryst. Growth*, 2000, **220**, 510–514.
15 Z. Galazka, S. Ganschow, K. Irmscher, D. Klimm, M. Albrecht, R. Schewski, M. Pietsch, T. Schulz, A. Dittmar, A. Kwasniewski, R. Grueneberg, S. B. Anooz, A. Popp, U. Juda, I. M. Hanke, T. Schroeder and M. Bickermann, *Prog. Cryst. Growth Charact.*, 2021, **67**, 100511.
16 K. Hoshikawa, E. Ohba, T. Kobayashi, J. Yanagisawa, C. Miyagawa and Y. Nakamura, *J. Cryst. Growth*, 2016, **447**, 36–41.
17 P. Li, Y. Bu, D. Chen, Q. Sai and H. Qi, *CrystEngComm*, 2021, **23**, 6300–6306.
18 B. Fu, W. Mu, J. Zhang, X. Wang, W. Zhuang, Y. Yin, Z. Jia and X. Tao, *CrystEngComm*, 2020, **22**, 5060–5066.
19 E. Villora, K. Shimamura, Y. Yoshikawa, K. Aoki and N. Ichinose, *J. Cryst. Growth*, 2004, **270**, 420–426.
20 B. Wang, D. Look and G. Farlow, *J. Phys. D: Appl. Phys.*, 2020, **53**, 444001.
21 Z. Galazka, R. Uecker, D. Klimm, K. Irmscher, M. Naumann, M. Pietsch, A. Kwasniewski, R. Bertram, S. Ganschow and M. Bickermann, *ECS J. Solid State Sci. Technol.*, 2017, **6**, Q3007–Q3011.
22 Z. Galazka, S. Ganschow, A. Fiedler, R. Bertram, D. Klimm, K. Irmscher, R. Schewski, M. Pietsch, M. Albrecht and M. Bickermann, *J. Cryst. Growth*, 2018, **486**, 82–90.
23 K. Hoshikawa, T. Kobayashi, Y. Matsuki, E. Ohba and T. Kobayashi, *J. Cryst. Growth*, 2020, **545**, 125724.
24 E. Ohba, T. Kobayashi, T. Taishi and K. Hoshikawa, *J. Cryst. Growth*, 2021, **556**, 125990.
25 D. J. Rogers, D. C. Look, F. H. Teherani, S. Yamakoshi, T. Masui, Y. Yamaoka, S. Watanabe, K. Koshi and A. Kuramata, *Oxide-based materials and devices IX*, 2018, 10533, UNSP 105330E.
26 J. Åhman, G. Svensson and J. Albertsson, *Acta Crystallogr., Sect. C: Cryst. Struct. Commun.*, 1996, **52**, 1336–1338.
27 E. G. Víllora, K. Shimamura, Y. Yoshikawa, T. Ujiie and K. Aoki, *Appl. Phys. Lett.*, 2008, **92**, 202120.
28 B. Fu, G. Jian, W. Mu, Y. Li, H. Wang, Z. Jia, Y. Li, S. Long, Y. Shi and X. Tao, *J. Alloys Compd.*, 2022, **896**, 162830.
29 W. Zhou, C. Xia, Q. Sai and H. Zhang, *Appl. Phys. Lett.*, 2017, **111**, 242103.
30 H. Cui, H. F. Mohamed, C. Xia, Q. Sai, W. Zhou, H. Qi, J. Zhao, J. Si and X. Ji, *J. Alloys Compd.*, 2019, **788**, 925–928.
31 C. V. Ramana, S. Roy, V. Zade, A. K. Battu, N. Makeswaran and V. Shutthanandan, *J. Phys. Chem. Solids*, 2021, **157**, 110174.
32 J. J. Sene, W. A. Zeltner and M. A. Anderson, *J. Phys. Chem. B*, 2003, **107**, 1597–1603.
33 L. Rossi, M. Palacio, P. I. Villabrille and J. A. Rosso, *Environ. Sci. Pollut. Res.*, 2021, **28**, 24112–24123.
34 H. Kim, A. Pique, J. Horwitz, H. Murata, Z. Kafafi, C. Gilmore and D. Chrisey, *Thin Solid Films*, 2000, **377**, 798–802.
35 J. Shao, W. Dong, D. Li, R. Tao, Z. Deng, T. Wang, G. Meng, S. Zhou and X. Fang, *Thin Solid Films*, 2010, **518**, 5288–5291.
36 L. El Mir, F. Ghribi, M. Hajiri, Z. B. Ayadi, K. Djessas, M. Cubukcu and H. J. von Bardeleben, *Thin Solid Films*, 2011, **519**, 5787–5791.
37 S. Lany, *APL Mater.*, 2018, **6**, 046103.
38 E. G. Víllora, K. Shimamura, Y. Yoshikawa, T. Ujiie and K. Aoki, *Appl. Phys. Lett.*, 2008, **92**, 202120.
39 N. Ueda, H. Hosono, R. Waseda and H. Kawazoe, *Appl. Phys. Lett.*, 1997, **70**, 3561–3563.
40 A. Navarro-Quezada, S. Alamé, N. Esser, J. Furthmüller, F. Bechstedt, Z. Galazka, D. Skuridina and P. Vogt, *Phys. Rev. B: Condens. Matter Mater. Phys.*, 2015, **92**, 195306.
41 N. Zhang, H. Liu, Q. Sai, C. Shao, C. Xia, L. Wan, Z. C. Feng and H. F. Mohamed, *J. Mater. Sci.*, 2021, **56**, 13178–13189.
42 R. Carli and C. L. Bianchi, *Appl. Surf. Sci.*, 1994, **74**, 99–102.
43 M. Chen, Z. Zhang, R. Zhan, J. She, S. Deng, N. Xu and J. Chen, *Appl. Surf. Sci.*, 2021, **554**, 149619.
44 I. López, A. D. Utrilla, E. Nogales, B. Méndez, J. Piqueras, A. Peche, J. Ramírez-Castellanos and J. M. González-Calbet, *J. Phys. Chem. C*, 2012, **116**, 3935–3943.
45 H. Cui, Q. Sai, H. Qi, J. Zhao, J. Si and M. Pan, *J. Mater. Sci.*, 2019, **54**, 12643–12649.
46 J. Huang, Y. Hu, T. Zou, K. Tang, Z. Zhang, Y. Ma, B. Li, L. Wang and Y. Lu, *Surf. Coat. Technol.*, 2019, **366**, 70–74.
47 Y. Li, J. Liu, D. Wang, G. Pan and Y. Dang, *Mater. Res. Bull.*, 2018, **100**, 220–225.
48 Z. Galazka, K. Irmscher, R. Schewski, I. M. Hanke, M. Pietsch, S. Ganschow, D. Klimm, A. Dittmar, A. Fiedler, T. Schroeder and M. Bickermann, *J. Cryst. Growth*, 2020, **529**, 125297.

View Article Online

49 A. Luchechko, V. Vasyltsiv, Y. Zhydachevskyy, M. Kushlyk, S. Ubizskii and A. Suchocki, *J. Phys. D: Appl. Phys.*, 2020, **53**, 354001.

50 V. Janakiraman, V. Tamilnayagam, R. S. Sundararajan, S. Suresh and C. S. Biju, *J. Mater. Sci.: Mater. Electron.*, 2020, **31**, 15477–15488.

51 D. Dohy, G. Lucazeau and A. Revcolevschi, *J. Solid State Chem.*, 1982, **45**, 180–192.

52 T. Onuma, S. Fujioka, T. Yamaguchi, Y. Itoh, M. Higashiwaki, K. Sasaki, T. Masui and T. Honda, *J. Cryst. Growth*, 2014, **401**, 330–333.

Published on 14 July 2022. Downloaded on 9/10/2022 9:58:10 AM.

This journal is © The Royal Society of Chemistry 2022